Available online at www.sciencedirect.com
ScienceDirect
Surface & Coatings Technology 202 (2008) 1951 – 1965
SURFACE & COATINGS TECHNOLOGY
www.elsevier.com/locate/surfcoat

Synthesis and characterization of laser-based direct metal deposited nano-particles reinforced surface coatings for industrial slurry erosion applications

Eswar Yarrapareddy, Radovan Kovacevic *

Center for Laser Aided Manufacturing Southern Methodist University 3101 Dyer Street, Dallas, TX 75206, USA

Received 22 January 2007; accepted in revised form 16 August 2007
Available online 29 August 2007

Abstract

A nano-based material system resistant to the impingement of solid and liquid particles on the solid surfaces was developed by the laser-based direct metal deposition (LBDMD) process. The nano-based materials system contains 5% tungsten carbide (WC) nano-particles that are agglomerated with nickel–tungsten carbide 60 (Ni–Tung 60) by ball mill operation for slurry erosion resistance applications. Slurry erosion tests are performed on the LBDMD processed depositions using the ceramic proppant at different impingement angles using the abrasive water jet erosion testing machine. From these tests the amount of material removed, depth of penetration, and profile of the formed crater are computed as a function of the abrasive water jet impingement angles. The nano-based materials system exhibited better performance for slurry erosion resistance than the monolithic Ni–Tung 60 depositions and 4140 steels. In order to understand the role of the WC nano-particles influence on slurry erosion resistance and to understand the characteristic features of erosion surfaces, sub-surfaces, and the erosion mechanism, different advanced characterization tools are used.

Keywords: Laser-based direct metal deposition; WC nano-particles; Slurry erosion; Characterization; Damage initiation and propagation

1. Introduction

In the industrial service applications, the high performance material systems play a vital role in deciding the properties such as high erosion resistance, high hardness, good mechanical strength, etc. These material systems fabrications are quite often challenging due to the high price of alloying elements and the high price of fabrication methods. However, these prices can be compensated by the longer life of the material systems. There have been many kinds of material systems available for industrial applications. However, the recent developments of the nano-based material systems have shown the proven results [1–8] in various applications.

In the recent years, the nano-based material systems have gained the interest of the research and industrial community. However, very limited research and development has been done using these material systems for industrial applications. The increase in wear resistance and hardness for nano-TiN/TiC/TiNi composites has been addressed by Luo et al. [1]. These composites are made by a vacuum sintering process using the pre-alloyed powders. Yu et al. reported the microstructures, hardness, and wear resistance of TaN/NbN nano-multilayers deposited by using the SPC-350 magnetron sputtering system [2]. The TaN/NbN multilayers exhibited the better wear resistance than the monolithic TaN or NbN single layer films. Agarwal et al. [3] studied the microstructural observations, wear, and friction behavior of hypereutectic aluminum based nano-structured composite surface coatings. These surface coatings were synthesized by a dry plasma spray technique by reinforcing the aluminum based surface coatings with carbon nano-tubes and nano-structured aluminum oxides.

Ji et al. confirmed that the nano-alumina particles are shown as promising filler materials for reducing the wear rate and the frictional coefficients of epoxy sliding against steel [4]. They also reported that the presence of nano-alumina accelerates the

* Corresponding author. Tel.: +1 214 768 4865; fax: +1 214 768 0812.
E-mail address: kovacevi@engr.smu.edu (R. Kovacevic).

0257-8972/$ - see front matter © 2007 Elsevier B.V. All rights reserved.
doi:10.1016/j.surfcoat.2007.08.032

epoxy curing process by the catalytic effect of hydrogen groups and the reduced free volume in the matrix. Chwa et al. prepared TiO_2 and TiO_2–Al composite coatings by plasma spraying using a reconstituted nano-sized feedstock via a spray drying method [5]. The wear loss of TiO_2–Al composite coatings was substantially decreased by the addition of nano-structured alumina powders. Gyftou et al. fabricated the Ni-based matrix composite coatings containing micron- and nano-sized SiC particles by a direct and pulse-plating regime technique to study the tribological behavior [6]. The presence of nano-sized SiC particles significantly enhanced the tribological performance. Cho et al. have done the experimental and numerical study on the effect of the particle size on elastic modulus, tensile strength, and particle/matrix debonding fracture toughness particulate composites [7]. They reported that Young's modulus and tensile strength of the particulate composite is not influenced by the micron or larger sized particles. However, the composite's Young's modulus and tensile strength has improved significantly by the addition of nano-sized particles. Xue et al. codeposited micrometer and nanometer La_2O_3 particles with nickel by electroplating from a nickel sulfate bath. They evaluated and studied the sliding wear of these coatings against AISI 1045 steel under non-lubricated conditions and found that nano-La_2O_3/Ni composite performed better for wear resistance than the micro-La_2O_3/Ni composite. Hence, there have been a number of investigations reported in literature for the tribological behavior of nano-reinforced materials systems fabricated by different manufacturing methods. However, there is no available literature on the fabrication of the surface coatings by the laser-based direct metal deposition (LBDMD) procedure. Hence, the authors focused on the research of synthesis and the characterization of the nano-particles reinforced surface coatings by the LBDMD process for the industrial slurry erosion applications.

The purpose of this work is the development of the best slurry erosion resistance material system for industrial applications. The LBDMD processed surface coatings are tested for slurry erosion at different impingement angles. The slurry erosion resistance is correlated to the microstructures and to the characteristic profiles of the craters formed. Furthermore, the slurry erosion resistance of the nano-based materials system is compared with that of the monolithic Ni–Tung 60 depositions and non-treated 4140 steel samples.

2. Materials

Four material system compositions are selected for the LBDMD process to study the slurry erosion resistance and to see how the nano-based material systems perform for the slurry erosion resistance. They are (i) Ni–Tung 60: contains micro-sized tungsten carbide particles that are uniformly distributed in a nickel-based matrix, (ii) 1% nano-WC + Ni–Tung 60: contains 1% nano-WC in Ni–Tung 60, (iii) 5% nano-WC + Ni–Tung 60: contains 5% nano-WC particles in Ni–Tung 60, and (iv) 10% nano-WC + Ni–Tung 60: contains 10% nano-WC particles in Ni–Tung 60. The chemical composition of Ni–Tung 60 is shown in Table 1. This powder is in a mesh size of −140+325 (100 to 145 um), and its apparent density is 7.8 g/cc and Rockwell hardness is 50 HRC. The nano-WC particles are in a

Table 1
The chemical composition of Ni–Tung 60

Element	C	Si	P	S	Cr	Mo	Co	Fe	B	W	Ni
Ni–Tung 60	2.80	1.39	0.006	0.001	0.24	0.03	0.02	0.1	0.58	57.22	Bal

Table 2
The chemical analysis of garnet

Ingredients	Percentage concentration
Silicon dioxide	41.34
Ferrous oxide	9.72
Ferric oxide	12.55
Aluminum oxide	20.36
Calcium oxide	2.97
Magnesium oxide	12.35
Manganese oxide	0.85

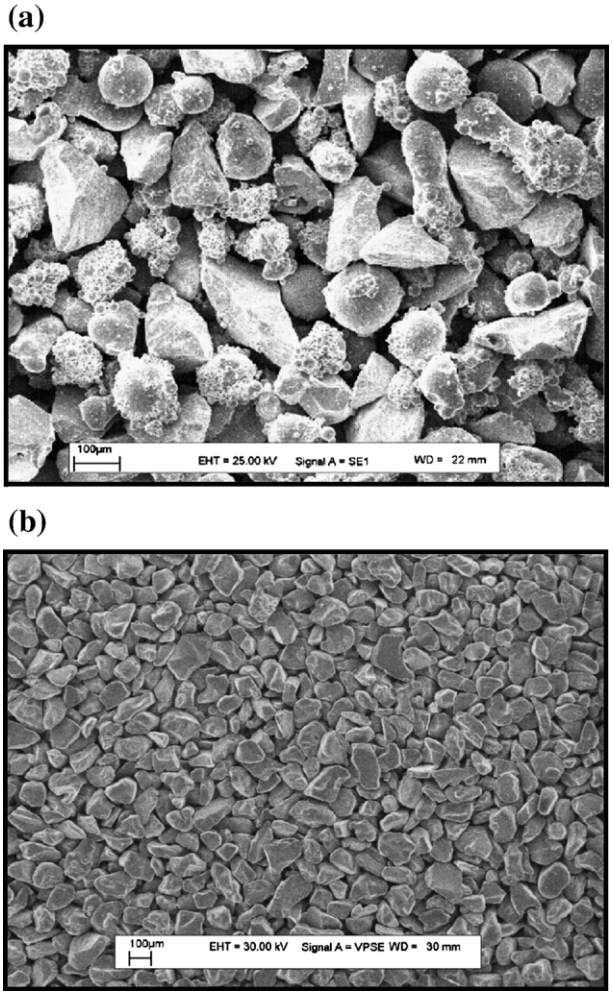

Fig. 1. The morphology of the (a) Ni–Tung 60 used for deposition and (b) the ceramic proppant (garnet) used for erosion testing. Note the difference in magnification between the micrographs.

size of 40 to 70 nm. An AISI 4140 steel coupons with the approximate dimensions of 30.4 mm (and 45.7 mm, 76.2 mm)× 25.4 mm×6.4 mm is used as a substrate for different size depositions. The chemical composition of AISI 4140 steel is 0.38–0.43 C, 0.75–1.00 Mn, 0.15–0.35 Mo, 0.8–1.10 Cr, max 0.035 P, max 0.04 Si, and the balance is Fe. Garnet was used as the abrasive material for the high pressure water jet for slurry erosion testing. The nominal chemical composition of this proppant is shown in Table 2, and its morphology is shown in Fig. 1(b). The garnet consists of homogeneous particles with uniform shape, narrow distribution, and no free chemicals.

3. Experimental procedures

3.1. Nano- and micro-powders agglomeration by ball mill operation

The mixing of nano-sized particles with micro-sized particles is a relatively new area of research. There are different procedures available in the literature [9–19] for mixing these powders. However, the authors applied a dry particle mixing procedure using the ceramic ball mill operation for mixing the nano-WC powders and Ni–Tung 60 micro-sized powders for about 1 h. These pre-mixed powders are observed under SEM to see the degree of mixing and homogeneity of nano-sized particles with the micro-sized particles. The morphologies of the pre-mixed powders are shown in Fig. 2. From these morphologies, it can be concluded that the 5% nano-WC with Ni–Tung 60 powder has a good degree of mixing. At this composition, the nano-WC particles are uniformly distributed and attached around the micro-sized particles. Based on the flowability of the powder mixtures as well as the obtained slurry erosion resistance of the buildups and degree of mixing, it is concluded that 5% nano-WC with Ni–Tung 60 performed very well for the deposition. Hence, further studies are performed on this material system composition. The flow chart illustrated in Fig. 3 shows the process, analysis, and characterization of the best slurry erosion resistant material systems developed by the LBDMD process.

3.2. The MultiFab system at SMU

The Center for Laser-Aided Manufacturing [previously part of The Research Center for Advanced Manufacturing (RCAM)],

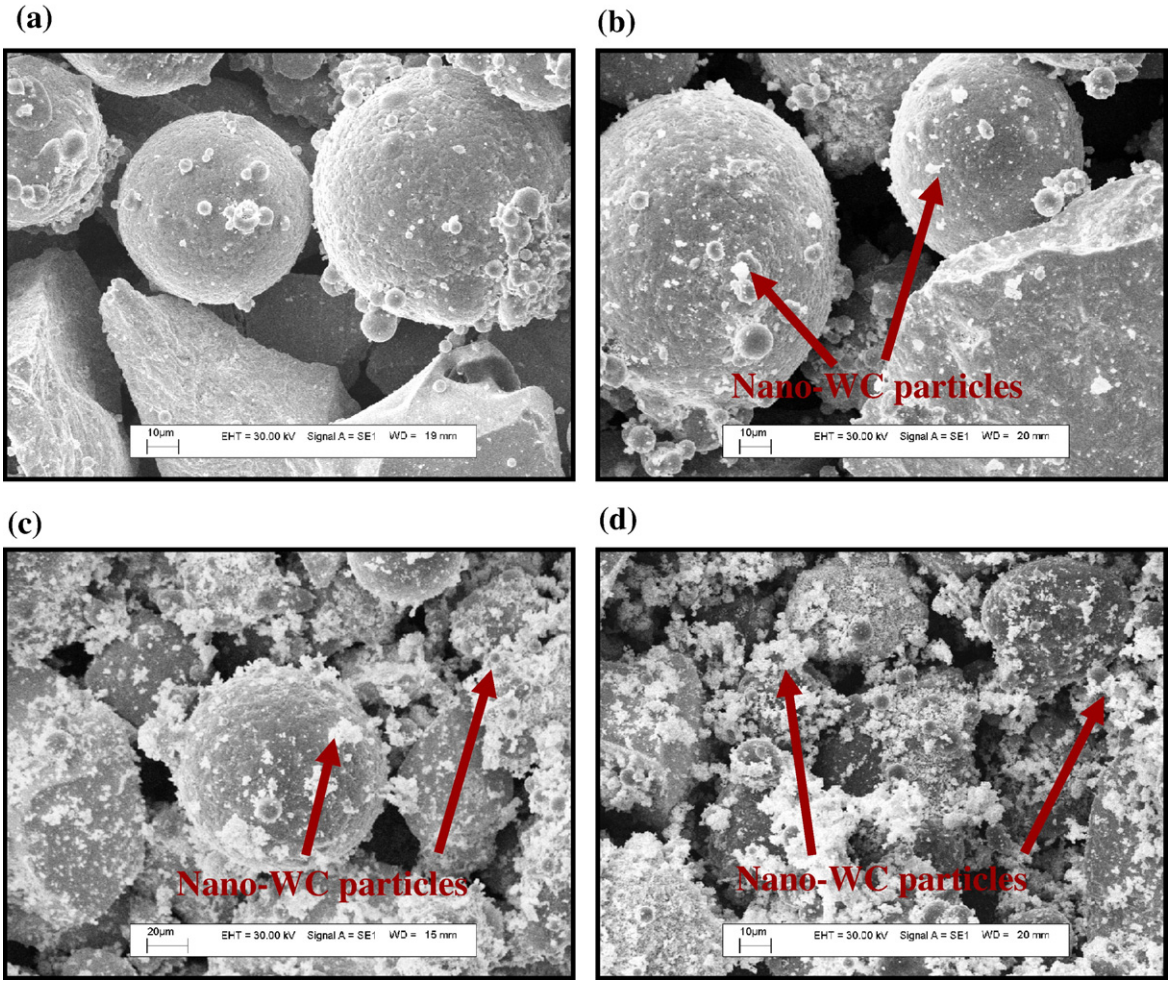

Fig. 2. The morphology of (a) the Ni–Tung 60 alloy powder and the agglomerated nano- and micro-powders with (b) 1% nano-WC, (c) 5% nano-WC (d) 10% nano-WC with Ni–Tung 60 used for deposition. Note the difference in magnification among the micrographs.

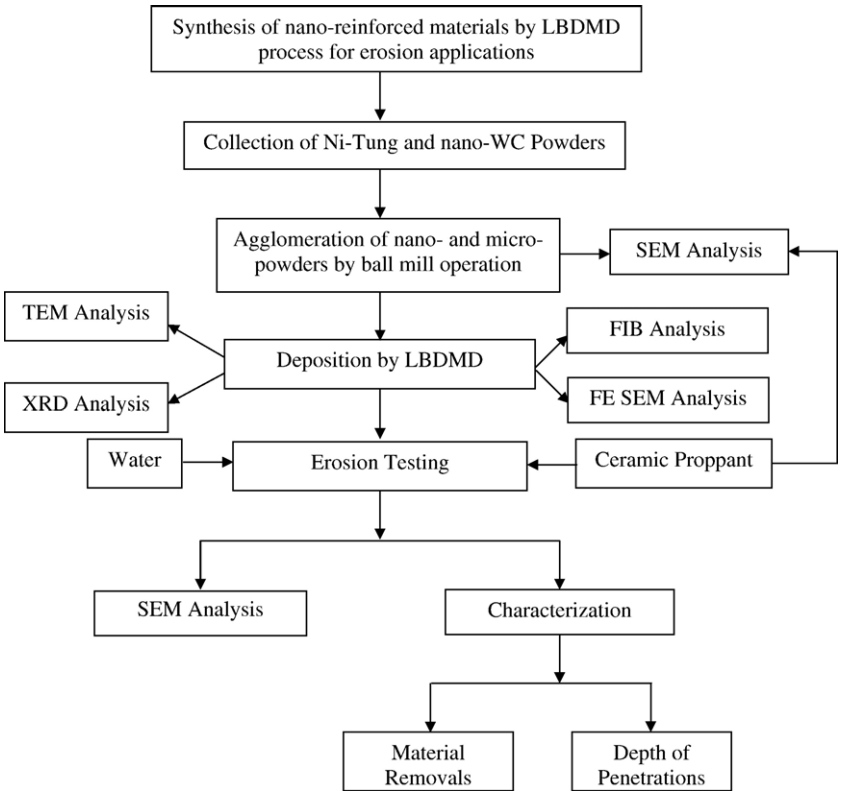

Fig. 3. Process, analysis and characterization flow chart for the synthesis of nano-particles reinforced materials system fabricated by LBDMD process.

at Southern Methodist University has been developing hybrid multi-functional equipment for rapid manufacturing (RM) and repair (Fig. 4). The Multi Fabrication (MultiFab) [20] system based on a combination of additive and subtractive techniques will provide the most concentrated part creation-and-repair ability in the world today. In the same setup on one computer-controlled platform, the following operations can be performed: two additive operations (deposition of metal by welding-based and laser-based additive process), subtractive operations (multi-axis computer numerical control — CNC milling, drilling, and tapping) and post-processing inspection.

The MultiFab system is composed of several subsystems. A 5-axis vertical CNC milling machine for positioning, milling, drilling, and taping with the 16-tool tool exchanger is the core of the MultiFab. A 6-axis UP6 Motoman robot with the most powerful PC based controller is used to carry and manipulate the micro-plasma welding deposition torch. A micro-plasma computer-controlled unit provides power and brings wire to the corresponding torch. A multimode laser beam for laser metal deposition is generated by the Nd: YAG laser unit with 1 kW of power in a continuous wave (CW) and 2.5 kW in a pulse mode. A laser beam is delivered to the laser head through a 1000-μm step index fiber-optic cable. The laser deposition head mounted on the CNC machine vertical axis is cooled by water. The deposition head is equipped with four radially symmetric nozzles at 30° with respect to the vertical axis. They deliver powder carried by an inert gas to the laser focal point (or molten pool). Two servo-motor driven powder feeders [21] that provide a stable powder flow are the key components of the powder delivery subsystem. The control system is based on a high-frame rate CCD camera and laser diode, both attached to the deposition head. The CCD camera, co-axial with respect to the

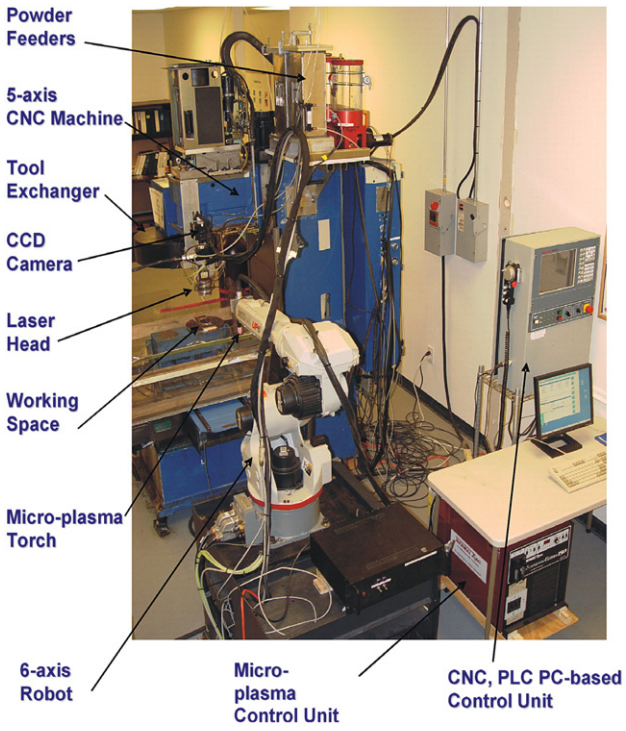

Fig. 4. The MultiFab system developed at the Center for Laser-Aided Manufacturing of SMU.

Table 3
The dimensions of the samples used for erosion testing

Impingement angle (degrees)	Dimensions of the LBDMD samples (mm)	Dimensions of the 4140 steel samples (mm)
15, 30	76.2×25.4×7.7	76.2×25.4×6.4
45, 60	45.7×25.4×7.7	45.7×25.4×6.4
75, 90	30.4×25.4×7.7	30.4×25.4×6.4

Table 4
The laser process parameters used for the depositing the four materials systems

Laser process parameter	Value
Laser power, p (watts)	350–380
Laser spot diameter, d (mm)	1
Linear traverse speed, v (mm/s)	8–10
Powder flow rate, f_p (g/min)	8–10
Gas flow rate, f_g (ft^3/h)	10–12
Layer height, h (mm)	0.43
Type of laser	Nd:YAG in continuous wave

laser beam, is equipped with an infrared (IR) filter to capture the shape of the molten pool in real time [22].

3.3. Surface coatings deposition procedure

The four material systems as shown Fig. 2 are deposited on 4140 steel substrate coupons using the LBDMD MultiFab system. Three layers of each materials system are deposited on the substrate to build the sample to an approximate size of 30.4 mm (and 45.7 mm, 76.2 mm)×25.4 mm×7.7 mm. These different sized samples are deposited to suit for their testing under the different impingement angles. These dimensions of the samples are illustrated in Table 3. The deposition profile used for all the material systems is shown in Fig. 5. These material systems are fabricated with a laser beam power of 350 to 380 W and a 1-mm diameter laser spot. Higher laser power is used for the first layer, and lower values are used for the second and successive layers. The linear traverse speed used is 8 to 10 mm/s, and the powder delivery speed is 8 to 10 g/min with argon as a powder carrier. Each layer is 0.43 mm in height and 1 mm in width. There is about a 40% overlap between the successive melting layers for all depositions in order to get the uniform surface of the built-up layer. These laser process parameters are summarized in Table 4.

3.4. Accelerated abrasive slurry erosion experiments

The accelerated abrasive erosion tests are conducted at room temperature using the high pressure water jet machine as shown in Fig. 6. In this machine, the motor-driven pump pressurizes the water and delivers it continuously to the cutting head. The ceramic abrasive materials called garnet with a fixed material shape is mixed with pressurized water in the cutting head. Then, the combination of the pressurized water and garnet turns into a supersonic abrasive water jet stream. This high pressure abrasive water jet stream impinged onto the test samples at different impingement angles. The metallic fixture for holding the different sized samples at different impingement angles relative to the water jet is shown in the Fig. 7. The water jet feeding orifice is 0.625 mm in diameter. The abrasive water jet that flows out of the pre-mixing nozzle first strikes the samples, then falls to the bottom of the reservoir. The excess water in the reservoir is filtered, then transferred to sewage. A pre-mixing nozzle provides a near-homogenous mixture of water and garnet components. The pre-mixing nozzle diameter is 1.02 mm. In order to decrease the speed of the mixture of abrasive and water, the stand-off distance is increased from 3 to 5 mm, which is regular for the classical abrasive water jet cutting, to 1127 mm that provides a uniformly dispersed mixture of water and abrasive particles.

For all experiments, the abrasive water jet concentration is maintained constant at all testing times. A series of experiments are carried out at different process parameters as illustrated in Table 5. The impingement angles are varied from 15 to 90° with an increment of 15° each time and impingement timing from 30 to 180 s. The abrasive flow rate is kept constant for all experiments at 4.3 g/s. The test samples are cleaned with methyl

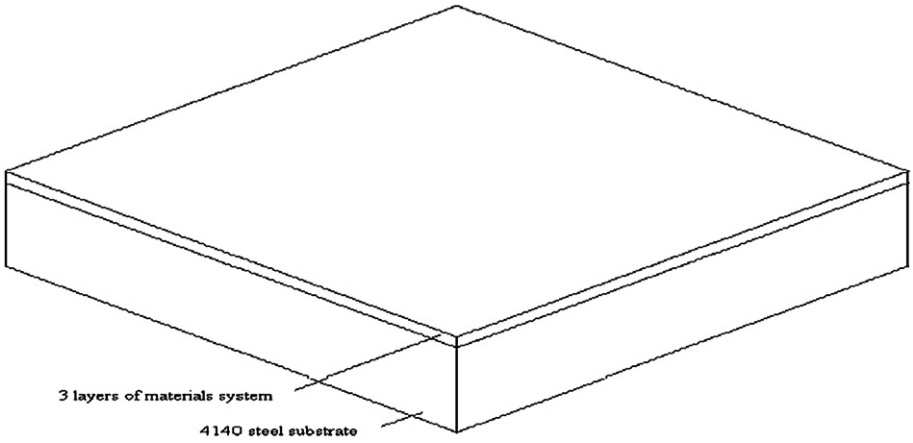

Fig. 5. The schematic representation of deposition profile used for fabricating the materials systems.

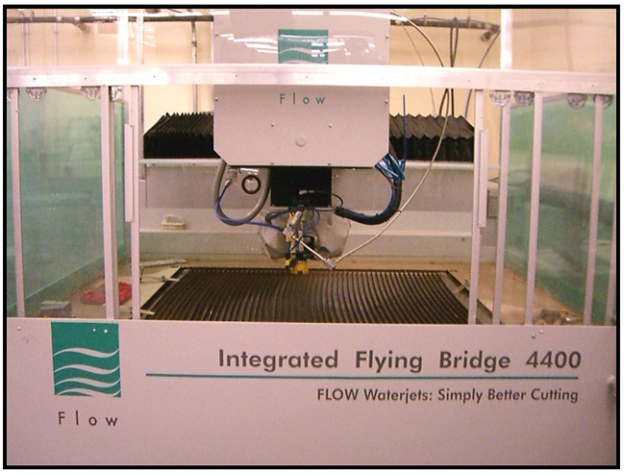

Fig. 6. The three-dimensional integrated flying bridge high pressure abrasive water jet machine.

alcohol before and after testing, and weighed for the weight loss using an electronic scale with an accuracy of 0.1 mg. Two experiments are used for each testing for accurate average weight loss values. The weight loss is calculated using the following formula.

$$\text{Weight Loss} = (W_i - W_f) \quad (1)$$

Where W_i is the initial weight of each sample, and W_f is the final weight after slurry erosion testing.

3.5. Microstructural characterization

The scanning electron microscopy (SEM) was performed for the ceramic garnet and pre-mixed powders to see the morphology using a Leo 1450 VP SEM equipped with an EDAX Genesis 4000 XMS system. The microscopy was performed at a voltage 20 to 30 kV and a working distance of 15 to 30 mm. The samples were glued to aluminum stubs, and the

Table 5
The process parameters and conditions for the abrasive erosion testing

Process parameter/condition	Value
Feeding nozzle diameter, D (mm)	0.625
Mixing tube diameter, D_t (mm)	1.02
Stand-off distance, H (mm)	1,127
Water pressure, p (ksi)	15, 25, 35, 45, 55
Erosion time, t (s)	30, 60, 90, 120, 150, 180
Impingement angle, α (degree)	15, 30, 45, 60, 75, 90
Abrasive type	Garnet with fixed shape
Abrasive particle size, d (μm)	80–100
Abrasive flow rate, m (g/s)	4.3

electrical contact between the stub and samples was made by carbon conducting tape. The field emission electron microscopy was performed at the University of Texas at Dallas using the state-of-the-art JEM 2100F FE SEM at a voltage of 5 to 20 KV. The focused ion beam (FIB) analysis was performed using the Nova 200 dual beam (FIB/SEM) with the ion source of liquid gallium metal. The analysis was carried out at a voltage ranging from 5 to 30 kV, a probe current ranging from 4 pA to 20 nA, and a beam aperture size ranging from 25 to 400 μm. The TLD secondary electron and backscattered electron detectors were used for imaging.

The X-ray diffraction patterns were recorded for perfectly flattened samples on the Rigaku Ultima III X-ray diffraction system. The diffractometer (Cu source and $\lambda = 1.5406$°A) is used for recording the patterns, and it is suitably designed for flat and thin sample surfaces. The absence of a perfect flat surface sometimes shifts the peak positions by about 0.5° at the lower 2θ angles, which results in wrong phase identifications. The high resolution TEM analysis was performed using the JEM-2100F field emission electron microscope. This machine has advanced features such as an ultrahigh resolution imaging camera and rapid data acquisition system. It has also a 200-keV field emission electron gun with automated apertures and stage maneuvering. The TEM samples are prepared using the FIB

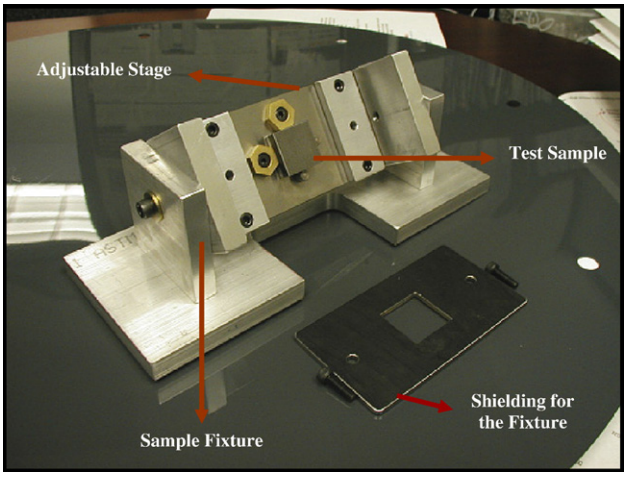

Fig. 7. The experimental set up used for the sample fixture showing the test sample, adjustable stage and shielding for the fixture.

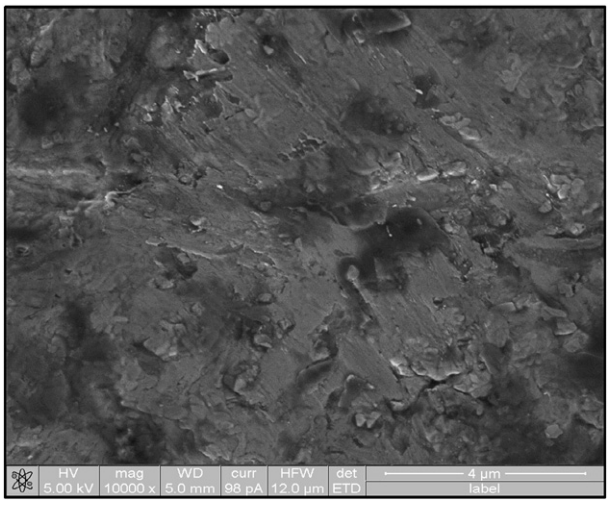

Fig. 8. The field emission SEM micrograph of homogenous and uniform distribution of Ni–Tung 60 after LBDMD process.

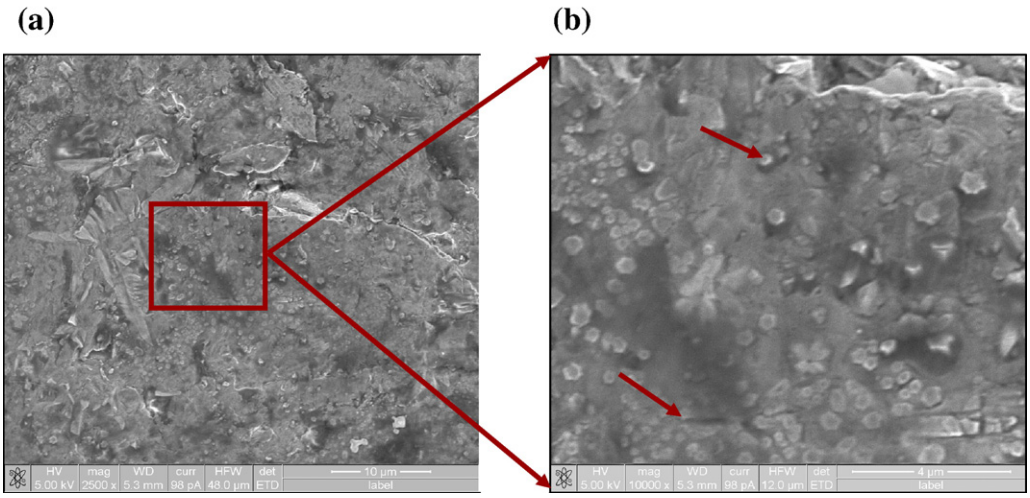

Fig. 9. The field emission SEM micrographs showing (a) the uniform and homogenous distribution of nano-size particles and (b) showing the higher magnification micrograph for nano-size particles filling space among the micro-size particles. Note the difference in magnification between the micrographs.

milling procedure. The average dwell time for each sample of 200-μm thickness took about 3 h.

4. Results and discussion

4.1. SEM characterization of pre-mixed nano- and micro-powders

The scanning electron microscopy (SEM) has been used for characterizing the ball mill pre-mixed and produced material systems. After each mixing experiment, the powder mixtures are examined under scanning electron microscopy. The SEM micrographs of the four material systems are shown in Fig. 2. The SEM micrograph in Fig. 2(a) shows the higher magnification image for Ni–Tung 60, showing the presence of micro-sized WC particles in a nickel-based matrix. The SEM micrograph in Fig. 2(b) shows the lesser amount of nano-sized WC particles among the micro-sized particles. In Fig. 2(c), the nano-sized WC particles are uniformly distributed, and there is a good degree of mixing showing a very distinct shape of micro-sized particles surrounded by nano-sized WC particles. Also, the nano-sized WC particles are either next to micro-sized particles or agglomerated. However, in Fig. 2(d), the nano-sized WC particles are non-uniformly distributed with un-even degree of mixing.

4.2. Morphology of Ni–Tung 60 after LBDMD process

The microstructural characteristics of Ni–Tung 60 after the LBDMD process are shown in Fig. 8. This microstructure is free from cracks and porosity. This is mainly due to the higher melting temperatures and rapid solidification procedures in the LBDMD process. Also, here the nickel-based matrix is strengthened by the reinforcement of WC particles. This microstructure also reveals that all the micro-sized particles are completely melted, and formed a homogeneous and uniform distribution of the particles after the LBDMD process was obtained.

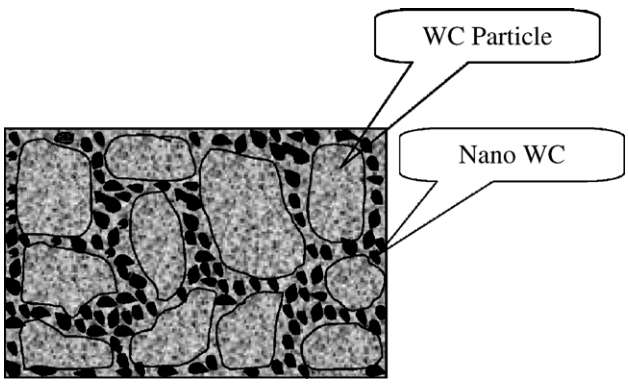

Fig. 10. The schematic representation of nano- and micro-size particles distributed after LBDMD process.

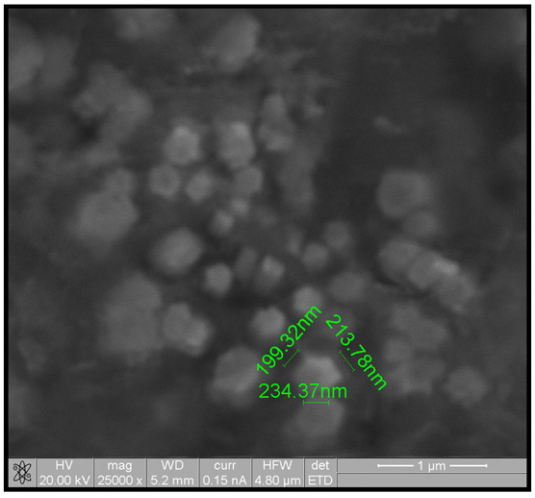

Fig. 11. The high magnification field emission SEM micrograph showing the nano-size particles size measurement after LBDMD process.

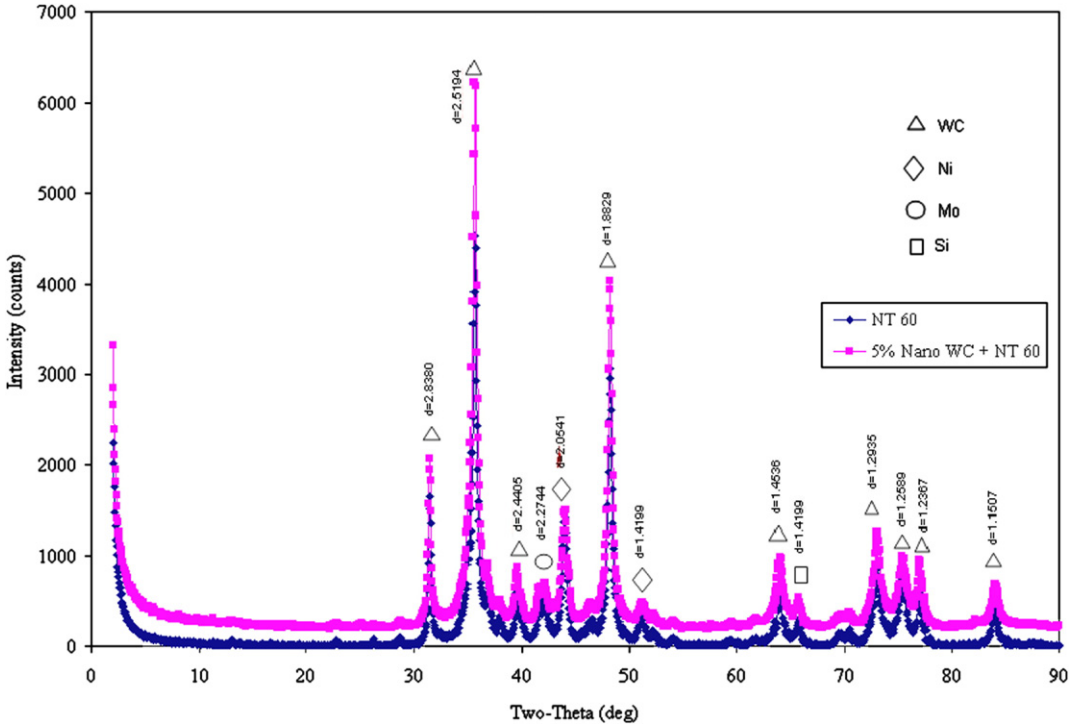

Fig. 12. The overlay of X-ray diffraction patterns showing for the Ni–Tung 60 and 5% nano-WC + Ni–Tung 60 after LBDMD process.

4.3. Morphology of 5% nano-WC + Ni–Tung 60 after LBDMD process

To further improve the strength of the Ni–Tung 60 matrix, the surface coatings are fabricated with 5% nano-WC particles reinforcement. The field emission SEM micrograph of 5% nano-WC + Ni–Tung 60 is shown the Fig. 9. Here, the nano-sized WC particles are uniformly distributed throughout the Ni-matrix, further giving strength to it. The nano-sized particles are shown with arrows in Fig. 9(b). Also, these nano-sized particles could further fill the space among the micro-sized grains after the LBDMD process. This filling further gives densification to the materials system, and it is schematically illustrated in Fig. 10.

Fig. 11 shows the micrograph for the 5% nano-WC + Ni–Tung 60 illustrating particles' size measurement after the LBDMD process. The size varied from 50 nm to 500 nm. For example, one of the measured mixtures of the particles size is shown in the Fig. 11. The size increase in the particles can be attributed to the agglomeration during the LBDMD process. Hence, those mixtures might vary from a single particle to a combination of particles. However, the high magnification single particles (grains) micrographs are illustrated in Section 4.6 using the TEM analysis.

4.4. X-ray diffraction results

Fig. 12 exhibits the XRD profiles for the Ni–Tung 60 and 5% nano-WC + Ni–Tung 60. It is found that by using the nano-sized particles for the reinforcement, the XRD spectrum is broadened, and the size of the nano-particles is decreased. The

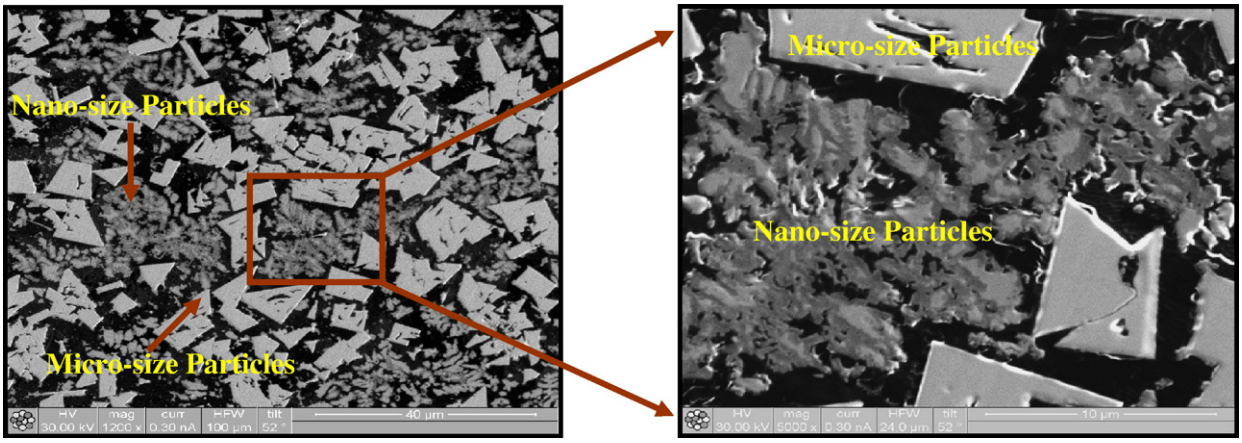

Fig. 13. The FIB micrographs showing (a) the nano-size grains around the micro-size grains after LBDMD process and (b) the higher magnification micrograph for Fig. 15(a). Note the difference in magnification between the micrographs.

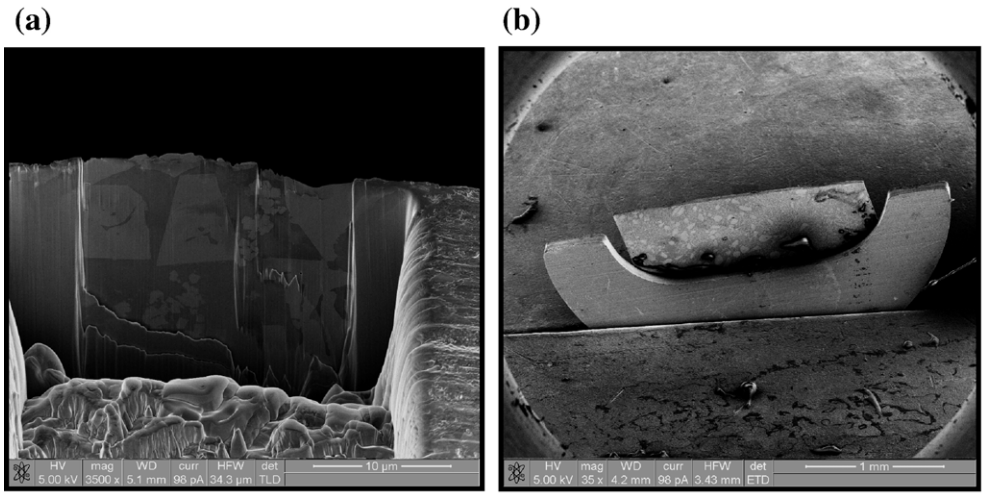

Fig. 14. The micrographs showing (a) FIB trench where the small sample cut from the bulk sample for lift-out and (b) the small sample mounted on the copper TEM grid for FIB thinning.

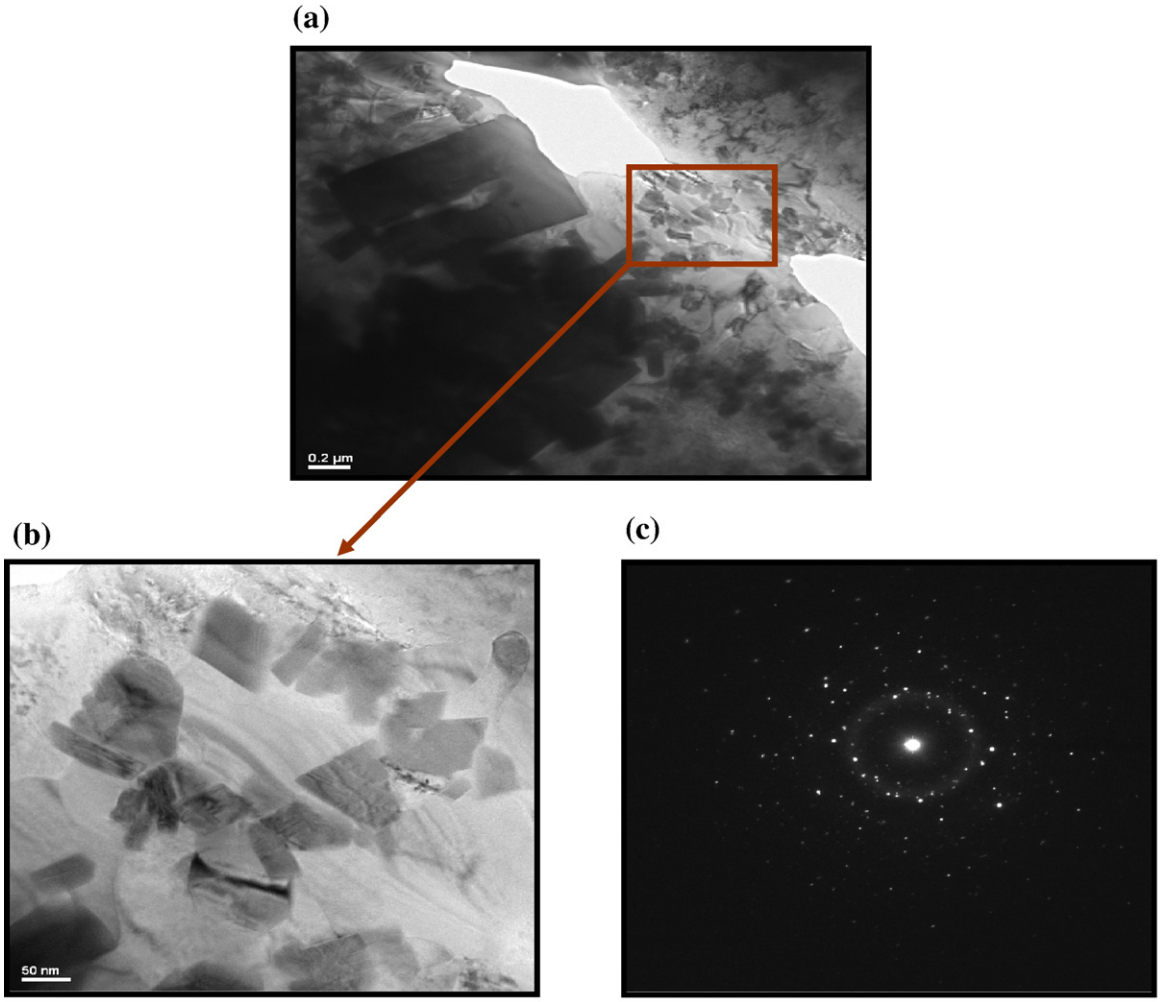

Fig. 15. The micrographs showing (a) the electron-transparent TEM sample prepared by FIB with the representation of TEM targeted area, (b) the high resolution bright-field TEM image showing the nano-size grains after LBDMD process and (c) the corresponding selected area diffraction pattern showing the corresponding bright reflections from nano-size grains.

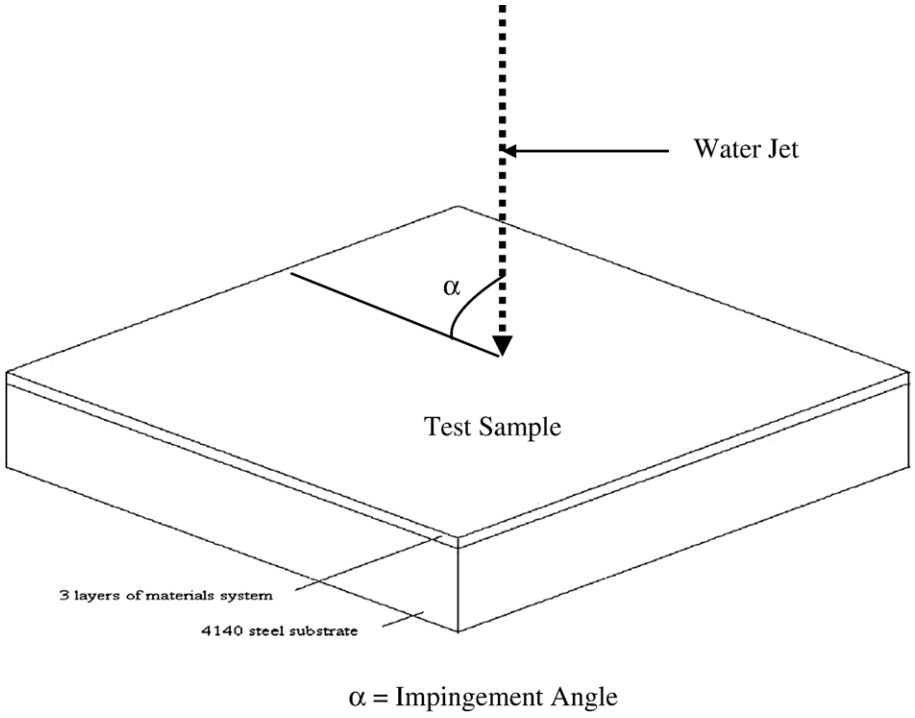

Fig. 16. The schematic representation of the impingement angle. α = 15°, 30°, 45°, 60°, 75°, 90°.

spectrum broadening is attributed to the higher content of WC particles in 5% nano-WC + Ni–Tung 60 than the content of particles in Ni–Tung 60. The size reduction of the nano-sized particles is attributed to the higher solidification temperatures and rapid cooling rates observed during the LBDMD process.

4.5. Focused ion beam (FIB) microstructural characterization

Fig. 13(a) shows the plain-view SEM micrograph of the 5% nano-WC + Ni–Tung 60 surface coating prepared by FIB milling. This micrograph shows the uniform grain structure with no detectable voids or delamination. Also, it can be observed that the nano-sized WC particles are homogeneously distributed throughout the matrix uniformly, providing further strength to it. These nano-WC particles either were completely melted or partially melted, providing solution strengthening to the matrix [23].

4.6. TEM analysis of 5% nano-WC + Ni–Tung 60

The TEM specimens are prepared using the focused ion beam sample preparation technique. A small sample of dimensions about 2 mm by 1 mm by 0.5 mm is cut from the bulk 5% nano-WC + Ni–Tung 60 sample by using the ultrasonic impact grinding tool as shown in Fig. 14(a). The small sample is then

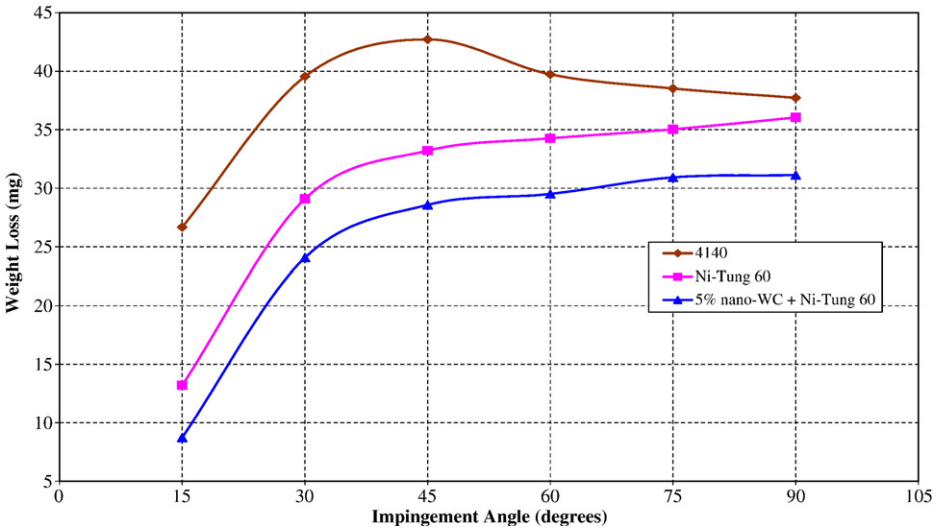

Fig. 17. The graph showing the weight loss values at different impingement angles for different tested materials.

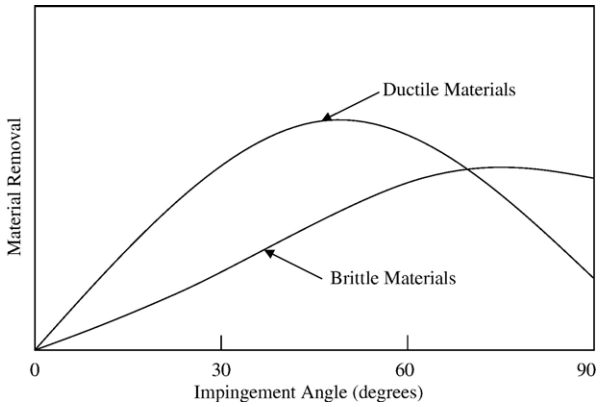

Fig. 18. Schematic representation of material removal on impingement angles for ductile and brittle materials [26].

polished by a tripod polisher for a flat surface. Then, the sample is mounted onto the copper TEM grid as shown in Fig. 14(b) for FIB milling. Then, it is loaded into the FIB microscope and milled carefully to 100 nm. The FIB milled and prepared electron-transparent TEM sample is shown in Fig. 15(a). Thus, with an FIB microscope, it is possible to focus on a small area out of the whole sample as wanted to be observed under the TEM. Hence, the authors used the undamaged area (represented with a box) for the TEM analysis. In this micrograph, one might see a damaged area that might have occurred during the FIB milling.

Fig. 15(b) represents a high resolution bright-field TEM image for 5% nano-WC + Ni–Tung 60. This microstructure shows the nano-sized WC grains uniformly distributed in the nickel matrix after the LBDMD process. The nano-sized WC grains are retained after the LBDMD process. The selected area diffraction (SAD) pattern illustrated in Fig. 15(c), shows the spotty ring pattern that is reflected from the nano-size grains. This kind of typical ring pattern is obvious from the nano-sized grains. These results further confirm the earlier microstructural and XRD results, and the idea of mixing nano-size particles with micro-size particles.

4.7. Slurry erosion test results

In order to evaluate the slurry erosion resistance of the samples made of 4140 steel, Ni–Tung 60 and 5% nano-WC + Ni–Tung 60 are blasted with a dispersed jet of water and garnet at different impingement angles as shown in Fig. 16. The graph showing the weight loss at different impingement angles is shown in Fig. 17. The weight loss values show that the 5% nano-WC + Ni–Tung 60 performs better than Ni–Tung 60 and 4140 steel at all impingement angles. At each impingement angle increment, the weight loss of the materials also increased gradually. However, in contrast to this weight loss, the ductile 4140 steel suffers the most severe erosion at an angle of 45°. This kind of characteristic feature is well known in dry erosion, where ductile materials usually show greater erosion at low impingement angles with respect to the brittle materials, and vice versa [24,25]. The schematic representation of ductile and brittle materials erosion resistance for different impingement angles is shown in Fig. 18 [26]. However, it is reported that such trends are less clear in the slurry erosion [24]. The excellent erosion resistance of 5% nano-WC + Ni–Tung 60 at all impingement angles is attributed to the matrix strengthening by the reinforcement of the nano-sized WC particles, and also these nano-sized particles fill the space around the micro-size particles as shown in the Fig. 13.

The maximum depth of penetration of the craters formed by the slurry erosion jet is measured by using a needle-shaped probe and a linear scale with a digital readout. Fig. 19 illustrates the depth of penetration profiles of the eroded craters formed for the 5% nano-WC + Ni–Tung 60, Ni–Tung 60 and 4140 steels after slurry erosion testing at different impingement angles. After each impingement angle, testing the distance between the

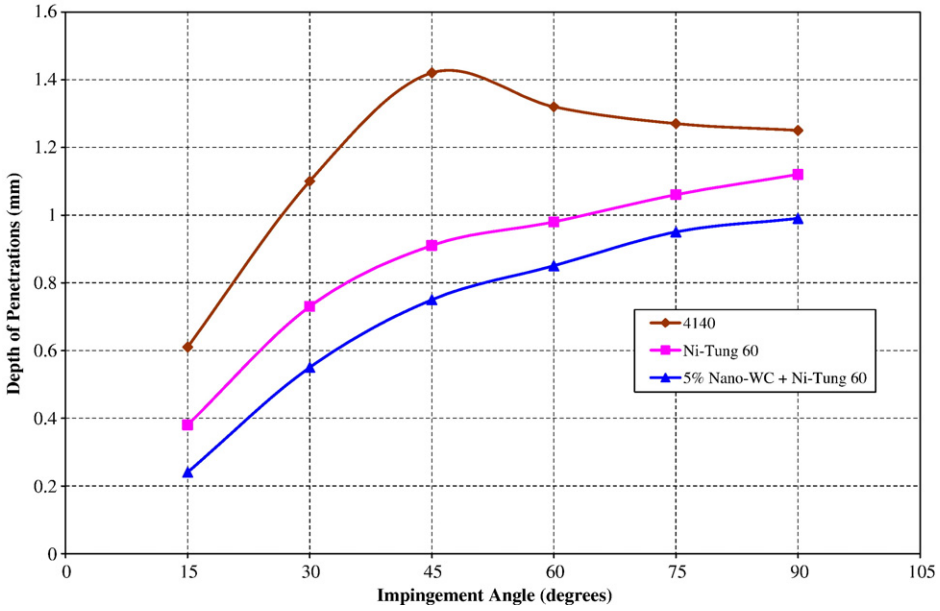

Fig. 19. The graph showing the maximum depth of penetrations of the tested materials as a function of different impingement angles.

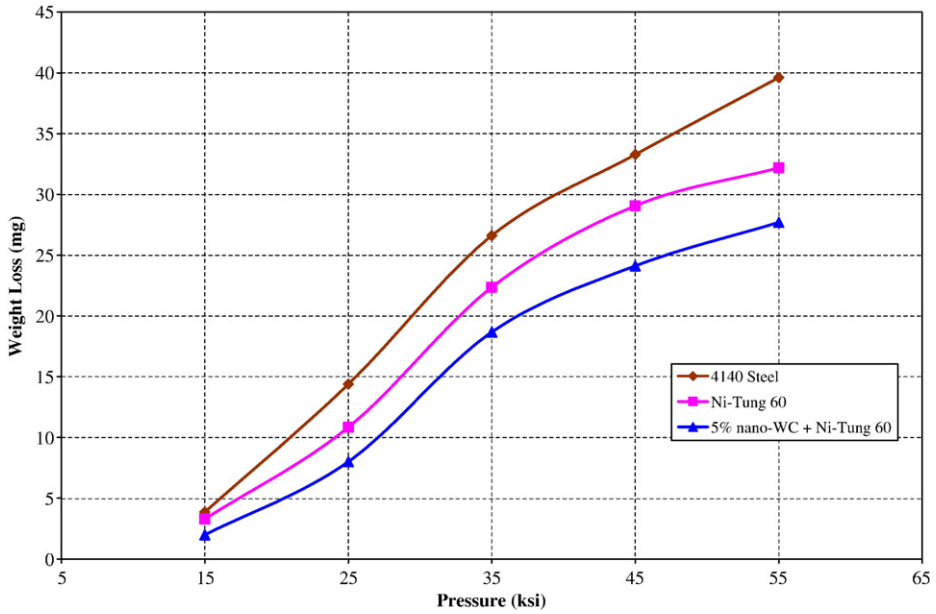

Fig. 20. The graph showing the weight loss values at different impingement water pressures for 45 degree impingement angle.

original surface and the eroded surface at the deepest position is measured, and it is termed as 'erosion depth of penetration'. For the 5% nano-WC + Ni–Tung 60, and Ni–Tung 60 materials surface coatings, the depth of penetration gradually increased with the increase in the impingement angle. However, for 4140 steel, the maximum depth of penetration is observed at a 45° impingement angle. This supports the earlier discussed weight loss measurements at the 45° impingement angle.

The effect of pressure of the water jet, *p,* which is directly proportional to the speed of the abrasive water jet on the slurry erosion weight loss, is shown in the Fig. 20. Here the samples are tested for erosion for 150 s at a 45° impingement angle. In this case, the higher the water jet pressure, the greater the weight loss from the material. For the water pressure between 45 ksi and 55 ksi, the erosion weight loss goes up heavily as the pressure increases. The relationship between the erosion weight loss and the erosion time at an impingement angle of 45° and a pressure of 55 ksi is illustrated in Fig. 21. The relationship can be approximately described as a linear relation. Irrespective of the material type, the amount of material loss is linearly increased as the impingement time increases.

4.8. SEM characterization of eroded surfaces

The eroded surfaces of the 5% nano-WC + Ni–Tung 60 and Ni–Tung 60 are characterized by scanning electron microscopy

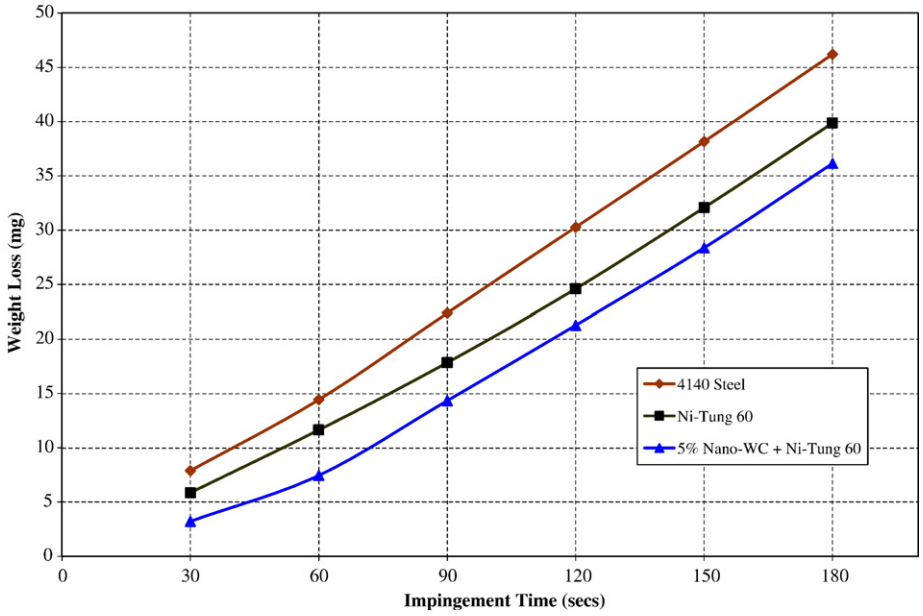

Fig. 21. The graph showing the weight loss values at 45 degree impingement angle with respect to different impingement timings for different tested materials.

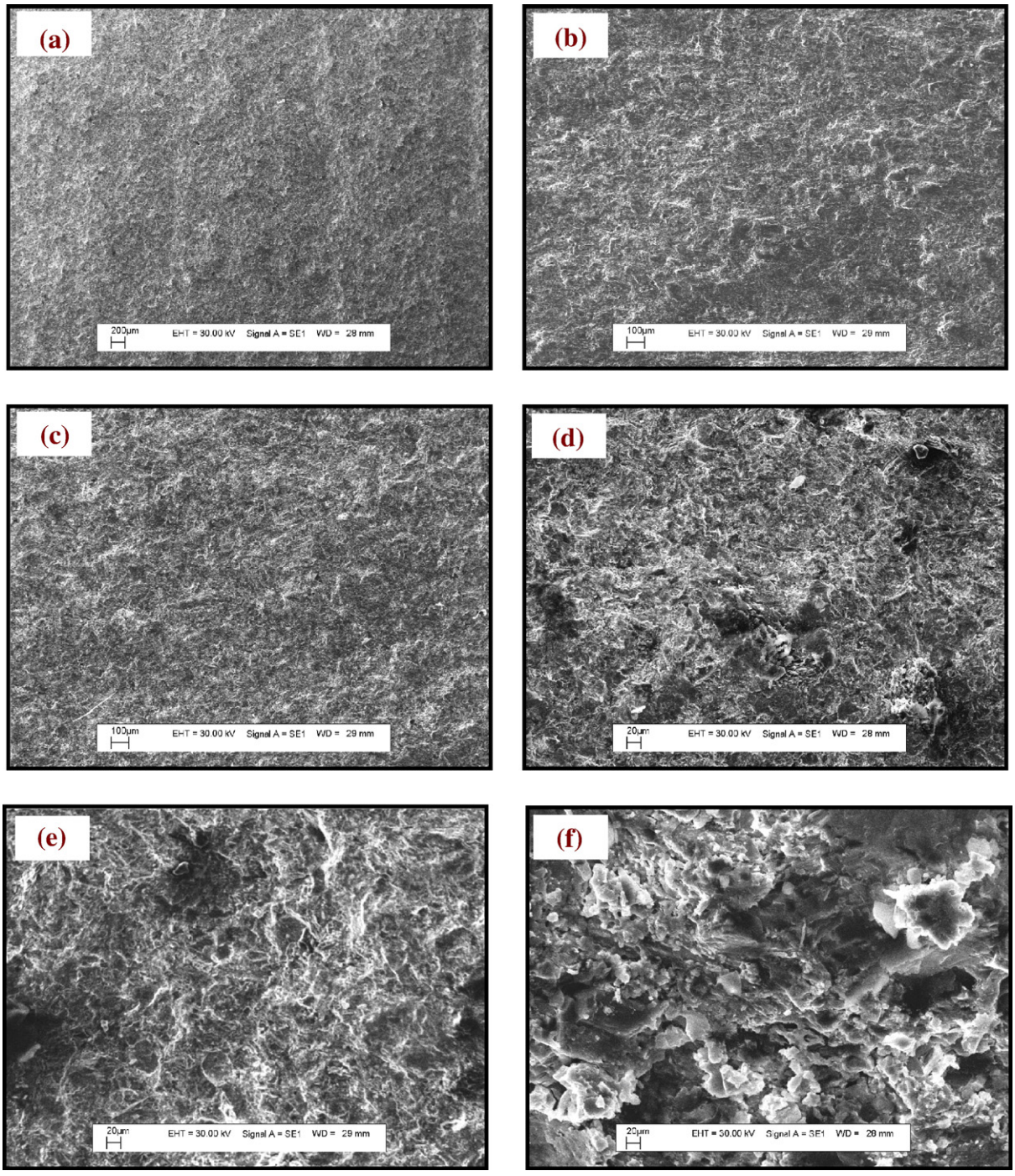

Fig. 22. The typical SEM microstructures of eroded Ni–Tung 60 samples tested at (a) 15° (b) 30° (c) 45° (d) 60° (e) 75° (f) 90° impingement angles. Note the difference in magnification among the micrographs due to difference in depth of penetrations of the craters.

in order to understand the characteristic features of erosion surfaces and sub-surfaces, and the erosion mechanism. The SEM micrographs for the eroded 4140 steels are reported elsewhere [27]. Figs. 22 and 23 show the morphology of the eroded surfaces of the 5% nano-WC + Ni–Tung 60 and Ni–Tung 60 at different impingement angles. The material removal and micro-cutting of the samples can be seen on the eroded surface morphologies. The material removal and micro-cutting occur on the samples when the plastic strain of the material exceeds its failure criteria value when that material is impacted by the high velocity water jet containing both the solid and liquid particles at different impingement angles. Hence, the damage is mainly initiated by the garnet and high pressure water jet particles. This damage is propagated for successive impingements of the garnet and water particles causing micro-cutting and material removal from the surface of the material.

At lower impingement angles, a lower number of pits and fewer micro cracks on the surface of the samples can be observed as shown in Figs. 22(a) and 23(a), impinged by a 15° angle of the abrasive water jet. At higher impingement

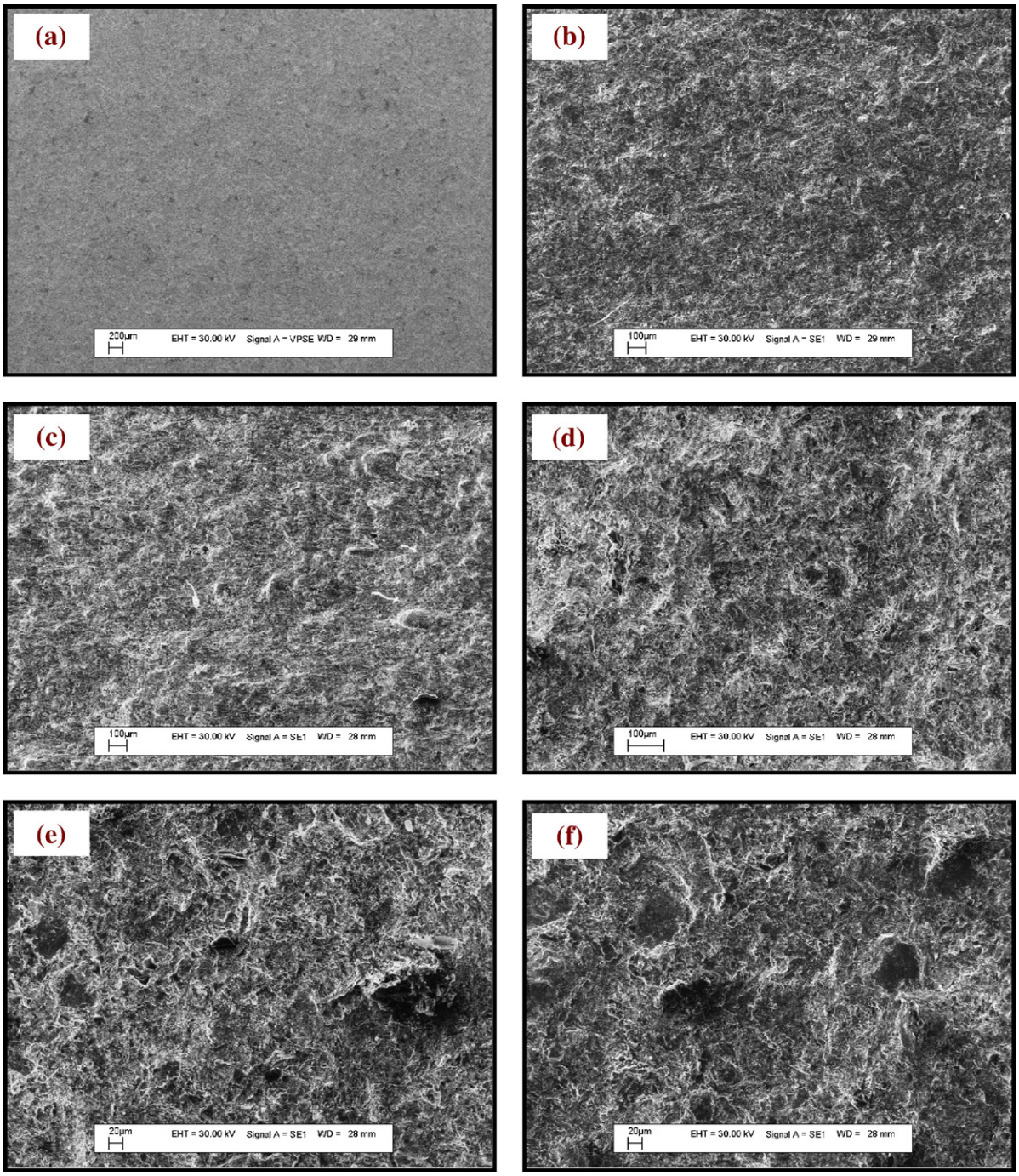

Fig. 23. The typical SEM microstructures of eroded 5% nano-WC + Ni–Tung 60 samples tested at (a) 15° (b) 30° (c) 45° (d) 60° (e) 75° (f) 90° impingement angles. Note the difference in magnification among the micrographs due to difference in depth of penetrations of the craters.

angles, an increasing number of pits and a high degree of micro-cutting of the material are present as shown in Fig. 22(f). However, in Fig. 23(f), there are fewer micro cracks and lesser materials removal on the surface morphology than the morphology in Fig. 22(f). This result implies that the reinforcement of Ni–Tung 60 with the nano-size WC particles can largely enhance the slurry erosion resistance. Hence, this enhancement is more significant in nano-reinforced samples than the micro-size samples. The application of nano-size WC particles as reinforcement for Ni–Tung 60 particles reduces the size of the Ni-crystalline matrix and increases the surface of the hard phase into the coating, which is manifest in the improvement of the slurry erosion resistance. Also, the reinforced nano-size particles in the matrix significantly enhance the jet impingement-bearing capacity of the 5% nano-WC + Ni–Tung 60 with respect to the monolithic Ni–Tung 60. The higher content of nano-WC particles composition in micro-sized particles could have the better slurry erosion resistance performance. However, to see this performance, further studies are needed.

5. Conclusions

The following conclusions can be made from the synthesis and the characterization of nano-reinforced surface coatings fabricated by the LBDMD process for slurry erosion resistance applications. The major findings can be summarized as follows.

- The nano-based materials system called 5% nano-WC + Ni–Tung 60 was successfully deposited by the LBDMD process.
- The average weight losses increase with an increase in the impingement angle, impingement time, and water pressure except for the samples made of 4140 steels at a 45° impingement angle. The 5% nano-WC + Ni–Tung 60 has the best slurry erosion resistance performance among the material systems tested. The eroded samples are characterized by analyzing the depth of penetration and performing the SEM analysis.
- Advanced characterization tools are used for the analysis of the surface coatings before and after slurry erosion testing.

Acknowledgements

The authors would like to acknowledge the financial support from Halliburton Energy Services through joining the NSF Industry University Co-operative Research Center Consortium (NSF Grant no. 0541952) for Laser-Aided Manufacturing program. The authors would like to acknowledge Dr. Moon Kim, Mr. Taehun Lee, and Mr. JB. Jeon of the University of Texas at Dallas for assisting in FIB and TEM analysis; Dr. Srdja Zekovic, Mr. Michael Valant and Mr. Andrew of SMU RCAM/CLAM for their help in performing the experiments; Dr. Syed Hamid and Dr. Haoyue Zhang of Halliburton Energy Services for technical discussions; and Mr. Roy Beavers of SMU for SEM and XRD support. The alloy powders and garnet are supplied by Carpenter Powder Products and Barton Mines Company, respectively. The slurry erosion experiments are performed on Flow International Corporation's accelerated abrasive water jet machine at SMU RCAM/CLAM.

References

[1] Y.C. Luo, D.Y. Li, J. Mater. Sci. 36 (2001) 4695.
[2] X. Yu, Q. Lai, G. Li, J. Xu, M. Gu, J. Mater. Sci. Lett. 21 (2002) 1671.
[3] A. Agarwal, K. Rea, S. Wannaparthun, S. Seal, N.B. Dhotre, T. McKechnie, Materials Science II, 2003, p. 81.
[4] Q.L. Ji, M.Q. Zhang, M.Z. Rong, B. Wetzel, K. Friedrich, J. Mater. Sci. 39 (2004) 6487.
[5] S.O. Chwa, D. Klein, C. Coddet, G. Bertrand, H. Liao, F.L. Toma, F.A. Belfort, A. Ohmori, Proceedings of the International Thermal Spray Conference, 10–12 May, Osaka, Japan, 2004, p. 837.
[6] P. Gyftou, M. Stroumbouli, E.A. Pavlatou, P. Asimidis, N. Spyrellis, Electrochim. Acta 50 (2005) 4544.
[7] J. Cho, M.S. Joshi, C.T. Sun, Compos. Sci. Technol. 66 (2006) 1941.
[8] Y. Xue, J. Li, W. Ma, M. Duan, J. Mater. Sci. 41 (2006) 1781.
[9] L.T. Fan, Y.M. Chen, F.S. Lai, Powder Technol. 61 (1990) 255.
[10] J.C. Williams, in: M. Rhodes (Ed.), Principles of Powders Technology, John Wiley & Sons, Chichester, 1990, p. 71.
[11] M. Poux, P. Fayolle, J. Bertrand, D. Bridoux, J. Bousquet, Powder Technol. 68 (3) (1991) 213.
[12] J.O.G. Parent, J. Iyengar, H. Henein, Int. J. Powder Metall. 29 (1993) 353.
[13] B.H. Kaye, Powder Mixing, Chapman & Hall, 1997, p. 19, 77–131.
[14] M. Rhodes, Introduction to particle technology, John Willey & Sons, West Sussex, 1998, p. 223.
[15] D. Myers, Surfaces, Interfaces, and Colloids: Principles and Applications, 2nd edition, Wiley-VCH, 1999, p. 40.
[16] K.J. Myers, M.F. Reeder, D. Ryan, G. Daly, Chem. Eng. Prog. (1999) 33.
[17] J.M. Ottino, D.V. Khakhar, Mixing and segregation of granular materials, 2000, Annual Revaluation Fluid Mechanics, vol. 32, 2000, p. 55.
[18] R. Weinekotter, H. Gericke, Mixing of Solids, Kluwer Academic Publishers, Dordrecht, The Netherlands, 2000, p. 15.
[19] D. Wei, R. Dave, R. Pfeiffer, J. Nanopart. Res. 4 (2002) 21.
[20] R. Kovacevic, M. Valant, "System and Method for Fabrication and Repairing Part," US Patent No. 7,020,539, issued on March 28, 2006.
[21] M. Valant, R. Kovacevic, "Powder Delivery System and Method," US Patent no. 7,045,738 issued on March 16, 2006.
[22] R. Kovacevic, D. Hu, M. Valant, "System and Method for Controlling the Size of the Molten Pool in Laser-based Additive Manufacturing," US Patent No. 6,995,334, issued on February 7, 2006.
[23] E. Yarrapareddy, S. Zekovic, S. Hamid, R. Kovacevic, Proceedings of the Institute of Mechanical Engineers—Part B, The Journal of Engineering Manufacture, vol. 220 (B12), 2006, p. 1923.
[24] H. Hawthorne, B. Arsenault, J. Immarigeon, J. Legoux, V. Parameswaran, Wear 225–229 (1999) 825.
[25] I. Finnie, Wear 19 (1972,) 81.
[26] C.G. Duan, V.Y. Karelin, Abrasive Erosion and Corrosion of Hydraulic Machinery, Imperial College Press, London, 2002, p. 242.
[27] E. Yarrapareddy, R. Kovacevic, "Numerical Simulation Charterization of Slurry Erosion of Laser Cladded Surfaces by Using Failure Analysis Approach", Submitted for ASM International's Journal of Failure Analysis and Prevention, May 2007, Article # JFAP-07-05-0116 (in press).